

Effect of the mean flow on the anomalous anticyclone over the Indo-Northwest Pacific in post-El Niño summers

Kaiming Hu^{1,2} • Gang Huang^{1,2,3} • Shang-Ping Xie⁴ • Shang-Min Long^{5,6}

Received: 21 February 2019 / Accepted: 5 July 2019 / Published online: 13 July 2019 © Springer-Verlag GmbH Germany, part of Springer Nature 2019

Abstract

A large-scale anomalous anticyclone (AAC) is a recurrent pattern in post-El Niño summers, extending from the tropical Northwest Pacific (NWP) to the North Indian Ocean. In boreal summer, there is a strongly confluent lower-level flow between the monsoonal westerlies and easterly trades over the Indo-Northwest Pacific. The effect of this basic state confluent flow on the AAC is investigated with energetics analysis and numerical modeling. The results show that the lower-level mean flow over the Indo-Northwest Pacific aids the AAC development. Specifically, the conversion of kinetic energy from the mean confluent flow to perturbations helps amplify easterly anomalies over the Indo-Northwest Pacific in post-El Niño summers. The enhanced easterly wind anomalies provide a positive feedback onto the AAC by inducing surface Ekman divergence to suppress convection over the NWP. Moreover, the structure of the optimal diabatic heating for the AAC pattern is determined using a method similar to the Green's function approach. The optimal forcing features heating in the tropical Indian Ocean and cooling in the NWP. This suggests that barotropic energy conversion in the confluence zone and the El Niño-induced positive (negative) sea surface temperature anomalies over the TIO (NWP) together lead to the AAC development over the Indo-Northwest Pacific in post-El Niño summers.

Keywords ENSO · East Asian Climate · Anomalous anticyclone

- ⊠ Kaiming Hu
 hkm@mail.iap.ac.cn
- State Key Laboratory of Numerical Modeling for Atmospheric Sciences and Geophysical Fluid Dynamics and Center for Monsoon System Research, Institute of Atmospheric Physics, Chinese Academy of Sciences, IAP/CAS, P.O. Box 9804, Beijing 100029, China
- Joint Center for Global Change Studies (JCGCS), Beijing 100875, China
- ³ Laboratory for Regional Oceanography and Numerical Modeling, Qingdao National Laboratory for Marine Science and Technology, Qingdao 266237, China
- Scripps Institution of Oceanography, University of California at San Diego, La Jolla, CA, USA
- College of Oceanography, Hohai University, Nanjing, China
- State Key Laboratory of Tropical Oceanography, South China Sea Institute of Oceanology, Chinese Academy of Sciences, Guangzhou, China

1 Introduction

El Niño-Southern Oscillation (ENSO) is the dominant mode of tropical interannual variability. It affects the climate around the globe through atmospheric teleconnections (Trenberth et al. 2002) and by inducing sea surface temperature (SST) responses in other ocean basins (Lau and Nath 1996; Klein et al. 1999). An anomalous anticyclone (AAC) often develops in the lower troposphere over the Indo-Northwest Pacific in boreal summer following an El Niño event (Fu and Ye 1988; Zhang et al. 1996; Wang et al. 2003), and is an important bridge that links ENSO to Asian climate. The El Niño-induced AAC is of great socioeconomic impact on populated regions of East, Southeast and South Asia. It weakens Northwest Pacific (NWP) summer monsoon by suppressing convection (Wang et al. 2000), enhances the East Asian summer monsoon by transporting moisture from the tropics (Chang et al. 2000), and decreases South Asian summer monsoon rainfall when extending westward to the northern parts of Indian (Chowdary et al. 2017). For example, anomalous southwesterly winds on the northwest flank of the AAC could cause floods in mountainous central China

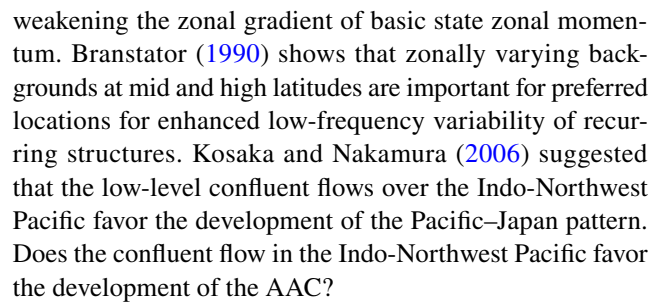


due to orographic lift (Hu et al. 2017). In addition, the AAC may result in warm summer in southern China and cool summer in northeastern China by modulating atmospheric circulation and precipitation (Hu et al. 2011, 2012).

The AAC in El Niño decaying summers is early revealed by Fu and Ye (1988) and found to be existent in 1986/1987 and 1991/1992 El Niño events by Zhang et al. (1996). The formation of AAC is considered to be linked with El Niñoinduced SST anomalies in other basins. In El Niño decaying summers, there is prominent SST warming in the tropical Indian Ocean (TIO) and slight cooling in parts of the NWP (Klein et al. 1999; Xie et al. 2002; Xiang et al. 2013; Jiang et al. 2017). The warming in the TIO could excite a warm tropospheric Kelvin wave propagating into the Western Pacific, induce Ekman divergence in the subtropical NWP to suppress convection, and trigger an AAC in the NWP (Xie et al. 2009), while the cooling in the NWP could lead to an AAC by suppressing local convection (Wang et al. 2003; Fan et al. 2013; Xiang et al. 2013; Jiang et al. 2017). The SST anomalies in different ocean basins may cooperate together to develop the AAC (Lau and Nath 2009; Wu et al. 2010; Xie et al. 2016). These SST anomalies over the TIO-NWP cooperate to maintain the AAC in summer, while recent studies (Stuecker et al. 2013, 2015; Zhang et al. 2016) suggested that the AAC initiation in preceding winter involves nonlinear interactions of ENSO and the background annual cycle (Xie and Zhou 2017).

In a modeling experiment by Kosaka et al. (2013) in which interannual variability is suppressed over the eastern equatorial Pacific, the AAC is still recurrent without involving ENSO process. Xie et al. (2016) demonstrated that the AAC could arise from inter-basin ocean–atmosphere feedback. The zonal contrast between the North Indian Ocean (NIO) warming and NWP cooling is in favor of an AAC. In return, an AAC further enhance NIO warming and NWP cooling through affecting evaporation and solar radiation. But in simulations from atmospheric general circulation model (AGCM) forced by climatological SST, the leading pattern of interannual atmospheric variability in the summer Indo-Northwest Pacific still features as an AAC (Zhou et al. 2018; Srinivas et al. 2018). This suggests that the AAC can arise from atmosphere-only process in absence of any coupling with ocean.

Questions arise: why does the AAC frequently appear over the Indo-Northwest Pacific in boreal summer? Is it related to the structure of the mean flow there? In summer, there is a strongly confluent lower level flow between the monsoonal westerlies and North Pacific easterlies. Such a climatological confluence zone favors zonally elongated perturbations due to kinetic energy conversion from the mean flow (Simmons et al. 1983; Branstator 1985, 1990; Kosaka and Nakamura 2006). The zonally elongated wind anomalies can gain kinetic energy from the confluence zone by



The present study investigates the role of the basic state in Indo-Northwest Pacific in the development of the AAC. We show that the strongly confluent lower-level mean flow over the Indo-Northwest Pacific helps anchor the AAC. The conversion of kinetic energy from the mean flow amplifies easterly anomalies over the Indo-Northwest Pacific in El Niño decaying summers. Furthermore, the enhanced easterly winds anomalies north of the equator can trigger the AAC by inducing surface Ekman divergence. Using a method similar to the Green's function approach (Branstator 1985) based on a linear atmospheric model, we show that deep atmospheric heating over the TIO and cooling over the NWP is the optimal atmospheric thermal forcing for the AAC pattern formation.

The rest of the paper is organized as follows. Section 2 describes the data and methods used in this paper. Section 3 examines the horizontal and vertical structure of atmospheric circulation anomalies in post-El Niño summers. Section 4 explores whether the summer basic state in the Indo-Northwest Pacific favors the development of the AAC through energetics analyses and numerical modeling. Section 5 discusses the role of moist feedback in the AAC development. Section 6 determines the optimal thermal forcing for the AAC. Section 7 is a summary with discussion.

2 Data and methods

Monthly mean winds, geopotential height, and air temperature are from the National Centers for the Environmental Prediction-Department of Energy (NCEP-DOE) atmospheric reanalysis (https://www.esrl.noaa.gov/psd/data/gridded/data.ncep.reanalysis2.html) at a resolution of 2.5° latitude × 2.5° longitude from 1979 to present (Kanamitsu et al. 2002). The Global Precipitation Climatology Project (GPCP; https://www.esrl.noaa.gov/psd/data/gridded/data.gpcp.html) monthly precipitation dataset is available from 1979 that combines gauge observations and satellite precipitation data into 2.5° latitude × 2.5° longitude global grid (Adler et al. 2003). The global gridded monthly SST dataset of the UK. Met Office Hadley Centre (HadISST; available at https://www.metoffice.gov.uk/hadobs/hadisst/) on a 1° latitude × 1° longitude grid is available from 1870



onward (Rayner et al. 2003). We use November–January mean (NDJ) Niño3.4 (5°S–5°N, 170°W–120°W) SST index to track ENSO, which is highly similar with the NDJ Niño3 index (not shown).

The linear baroclinic model (LBM) used in this study consists of primitive equations linearized about a given basic state. The model has a horizontal resolution of T42 and 20 vertical levels based on the sigma coordinate system, a horizontal (vertical) diffusion, Rayleigh friction, and Newtonian damping. The horizontal diffusion has a damping time scales of 6 h for the smallest wave, and the Rayleigh friction and Newtonian damping have a time scale of 1 day⁻¹ for sigma levels below 0.9, (5 day)⁻¹ for sigma level of 0.89, (15 day)⁻¹ for sigma level of 0.83, (30 day)⁻¹ for sigma level between 0.83 and 0.03, and 1 day⁻¹ for sigma levels above 0.03. The diffusion and damping coefficients are the default values in the LBM. Details of the model formulation are given in Watanabe and Kimoto (2000). In this study, we use the dry version of the LBM to study the linear atmospheric responses to different thermal forcing and basic states. To obtain the steady atmospheric response to forcing, the model is integrated for 50 days, and the averages from 20 to 50 days are used. Simmons et al. (1983) showed that the outcome of a linear model is somewhat sensitive to the choice of diffusion and damping coefficient. So, we also test the sensitivity of the LBM's results to the choice of diffusion and damping coefficient, and found that the spatial structure of the LBM's results is not sensitive to exact values (figure not shown).

3 Atmospheric circulation anomalies in post-El Niño summers

Figure 1a shows the regression of JJA (June–July–August)mean 850-hPa winds and the correlation of rainfall and of vertically averaged air temperature in the free troposphere (from 850 to 200-hPa) with the preceding NDJ Niño3.4 SST index during 1979-2016. Consistent with previous studies (Wang et al. 2003; Xie et al. 2009), the strongest surface atmospheric anomalies appear over the Indo-Northwest Pacific, including decreased rainfall and an anomalous anticyclone. On the south flank of the AAC, strong easterly anomalies develop from the International Date Line to the Arabian Sea. Hereafter, this atmospheric circulation anomaly pattern is referred to as the AAC pattern. Tropospheric temperature displays a Matsuno (1966) and Gill (1980) pattern with the maximum correlation over the eastern TIO. A Kelvin wave wedge penetrates into the Western Pacific along the equator and two off-equatorial Rossby wave tails over Africa and the western Indian Ocean. These results are consistent with the Kelvin wave-induced Ekman divergence mechanism of Xie et al. (2009) for the AAC pattern.

Figure 1b shows the latitude-height section of JJA 90°-150°E averaged air temperature and zonal wind anomalies regressed onto the preceding NDJ Niño3.4 SST index.

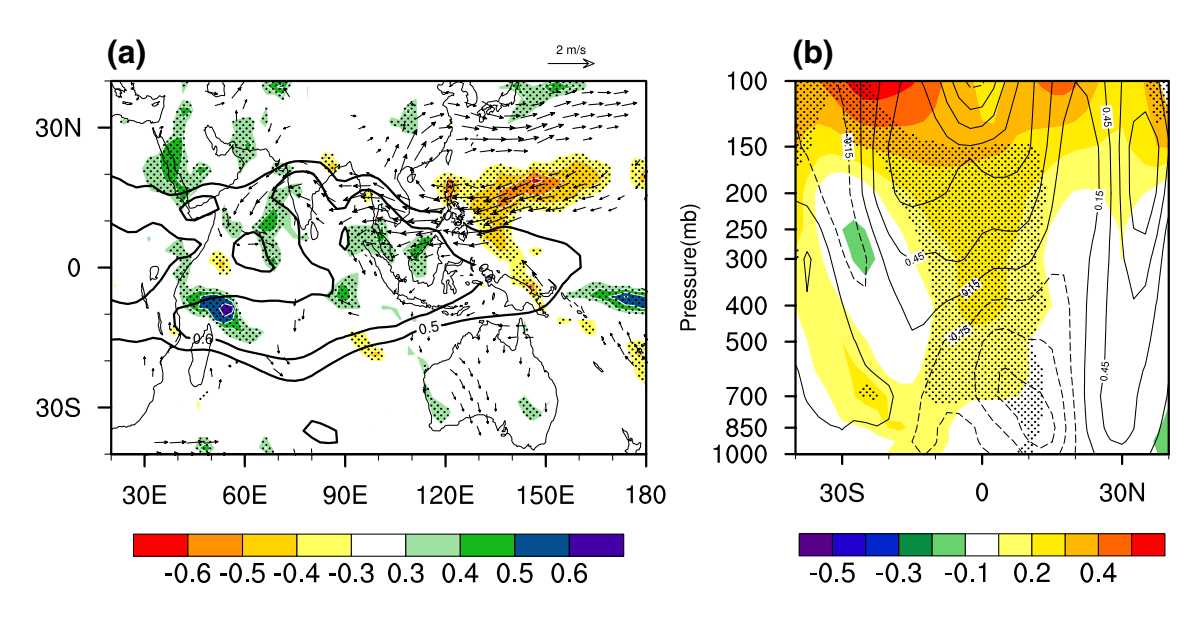


Fig. 1 a Correlation of JJA precipitation (colors) and vertically averaged (850–200 hPa) air temperature (contours) with and regression (vectors, ms⁻¹) of 850-hPa winds onto the normalized preceding NDJ Niño3.4 SST index. **b** Height-latitude section of 90°–150°E averaged air temperature anomalies (colors, k) and zonal wind anomalies (con-

tours, interval at $0.3~{\rm ms}^{-1}$) regressed onto the normalized preceding NDJ Niño3.4 SST index. Shading denotes the correlations or anomalies passing the 95% confidence level. Only the anomalous winds exceeding the 95% confidence level are shown



In the tropics, there are easterly (westerly) wind anomalies below (above) the level around 400-hPa and positive temperature anomalies throughout the troposphere. Both the westerly wind and air temperature anomalies above 600 hPa are nearly symmetric about the equator, indicative of the Kelvin wave structure. In the lower troposphere by contrast, easterly anomalies are much stronger north than south of the equator, suggesting that the asymmetry of atmospheric anomalies is mainly confined at the lower troposphere.

4 The effect of summer basic state

This section investigates in two steps whether the confluence zone over the Indo-Northwest Pacific facilitates the development of the AAC pattern. First, we conduct energetics analyses to show that the AAC gains energy from the mean flow in observations. Second, we illustrate the effect of the basic state on the AAC with LBM simulations. The method used in this section is linear, so it can also be applied to the case with westerly wind perturbations that appear in La

Nina's cases. For simplicity, we only discussed the effect of basic state on the easterly wind anomalies in post-El Niño summers in this study.

a. Energetics analyses

Following Kosaka and Nakamura (2006), the barotropic growth of the local kinetic energy (KE) associated with perturbations from the basic state is given by

$$\frac{\partial KEH}{\partial t} \approx \underbrace{\frac{(v'^2 - u'^2)}{2} \left(\frac{\partial u_b}{\partial x} - \frac{\partial v_b}{\partial y} \right)}_{CKx} - \underbrace{u'v' \left(\frac{\partial u_b}{\partial y} + \frac{\partial v_b}{\partial x} \right)}_{CKy}, \tag{1}$$

$$CK = CKx + CKy, (2)$$

$$KEH = (u'^2 + v'^2)/2.$$
 (3)

Here u' and v' are the anomalous 850-hPa zonal and meridional winds shown in the Fig. 1a, u_b is the observed climatological JJA winds at 850-hPa shown in Fig. 2a, KEH is horizontal perturbed kinetic energy, and CK is conversion of local kinetic energy from the basic state to perturbations. Positive conversion of local kinetic energy means perturbations gain kinetic energy from the mean flow. The Eq. (1) is

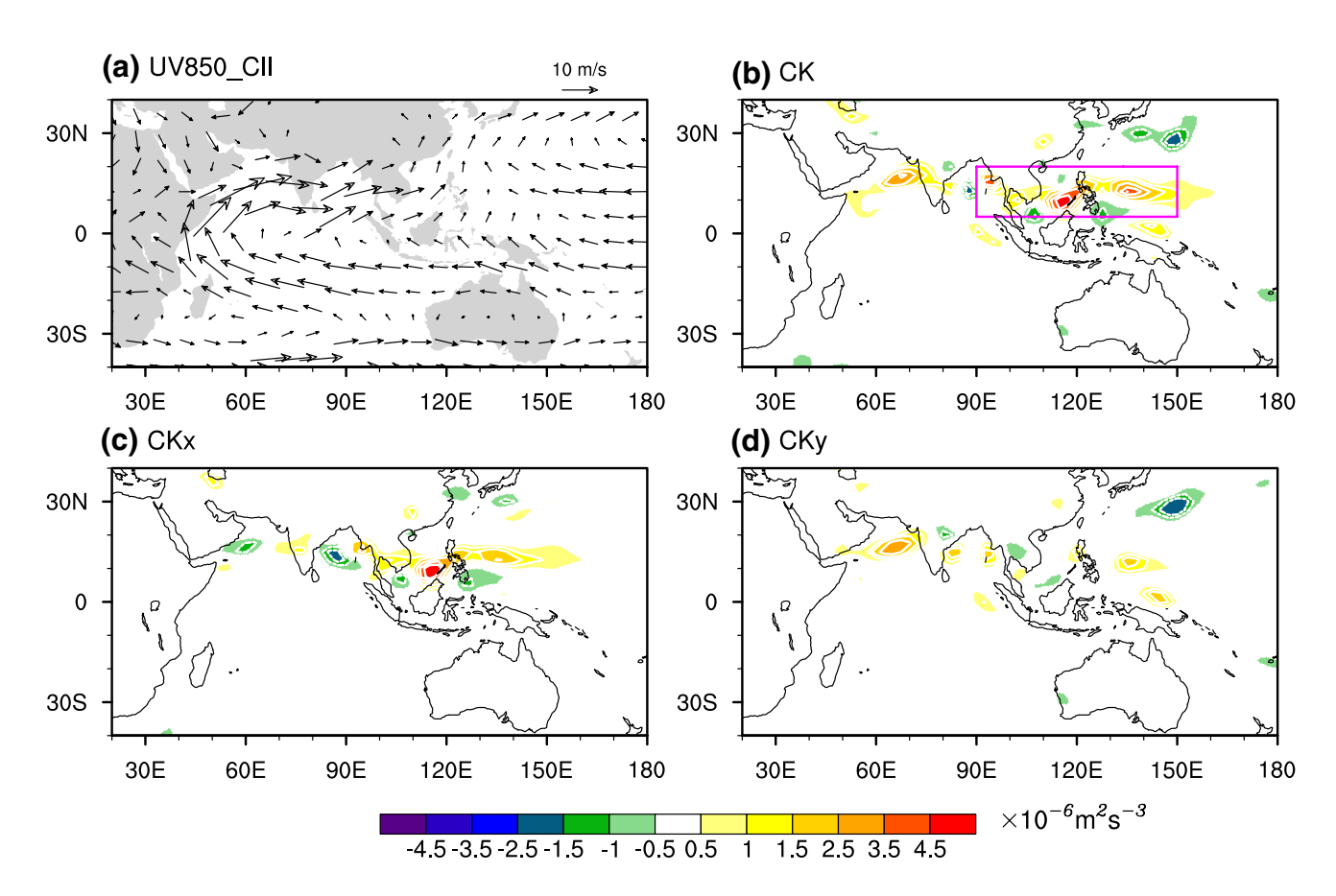


Fig. 2 a JJA 850-hPa wind climatology (vectors). **b** Conversion of kinetic energy (*CK*) at 850 hPa from the basic state to perturbations based on the Eq. (1). The first **c** and second **d** parts of *CK* at 850 hPa in the Eq. (1)



also the same as that in Simmons et al. (1983) if the mean flow is considered non-divergent.

Figure 2a show the climatological (1979–2015) JJA-mean horizontal winds at 850-hPa in the observations. There are strong southwest monsoon winds from the NIO to East Asia and strong easterly trades from the central Pacific. The monsoon and trade winds converge into a broad confluence zone over the Indo-Northwest Pacific. Here the confluence zone refers to the region of negative $\frac{\partial u_b}{\partial x}$. For simplicity, we set the confluence zone as the region of 5° –20°N, 90° –150°E. According to the Eq. (1), zonally elongated circulation anomalies ($u'^2 > v'^2$) can induce positive CK in a region of zonal flow confluence. Consistent with this theoretical prediction, the CK is positive in the confluence zone (Fig. 2b), suggesting that the AAC in post-El Niño summers gains kinetic energy from the mean flow.

In the Eq. (2), CK can be divided into two parts: CKx and CKy. The first part (CKx) represents the conversion of kinetic energy between a mean confluent flow and perturbations, while the second part (CKy) denotes the conversion between a mean horizontal shear and perturbations. The maximum positive CKx is distributed from the NWP to the east of the Bay of Bengal (Fig. 2c) which is consistent with the prominent zonal confluence there, while the maximum positive CKy is located over the Arabian Sea (Fig. 2c). The area-mean CK, CKx and CKy over the zonal confluence zone (5°–20°N, $70^{\circ}-150^{\circ}$ E) are $0.68 \times 10^{-6} \text{ m}^{-2}\text{s}^{-3}$, $0.56 \times 10^{-6} \text{ m}^{-2}\text{s}^{-3}$, and $0.12 \times 10^{-6} \,\mathrm{m}^{-2}\mathrm{s}^{-3}$, respectively, indicating CKx plays a dominant role in the total conversion of local kinetic energy across this region. To measure the efficiency of CK in maintaining of the easterly wind anomalies in the south flank of the AAC, we evaluate the time scale: $\tau_{CK} = \frac{\langle KEH \rangle}{\langle CK \rangle}$, where the bracket $\langle \rangle$ represents area mean over 5°-20°N, 90°-150°E. The value of τ_{CK} denotes how long it takes for the kinetic energy of perturbations to be fully replenished through CK. The τ_{CK} is 4.8 days, which may be efficient enough to counter damping processes there.

Note that the Eq. (1) does not include the redistribution of kinetic energy from one place to another (Lau and Lau 1992). In a baroclinic system, the local eddy kinetic energy balance equation is written as

$$\frac{\partial KE}{\partial t} = \underbrace{\frac{(v'^2 - u'^2)}{2} \left(\frac{\partial u_b}{\partial x} - \frac{\partial v_b}{\partial y}\right) - u'v' \left(\frac{\partial u_b}{\partial y} + \frac{\partial v_b}{\partial x}\right)}_{CK}$$

$$- \underline{u' + u_b \left(\frac{\partial KE}{\partial x}\right) - v' + v_b \left(\frac{\partial KE}{\partial y}\right)}_{KA}$$

$$- \underbrace{\frac{R}{P}\omega'T'}_{KP} - \underline{u'}\frac{\partial \Phi'}{\partial x} - v'\frac{\partial \Phi'}{\partial y} - \omega'\frac{\partial \Phi'}{\partial P} + KR.$$
(4)

Here, u', v', u_h , v_h and KE is similar to that in the Eq. (1) but for all levels, P is atmospheric pressure, T' is anomalous air temperature, Φ' is anomalous geopotential height, and ω' is anomalous vertical velocity. The equation is similar to that used in Lau and Lau (1992). The only difference is that a time-mean operator was added in each term in Lau and Lau (1992) analyses, as it was used to diagnosis the transient eddy kinetic energy balance. According to Lau and Lau (1992), the term CK denotes the barotropic conversion of perturbed kinetic energy from the basic state, which is the same as that in the Eq. (1). The term KA represents the advection of perturbed kinetic energy by the horizontal timemean and perturbed flow. The term KP describes the conversion from perturbed available potential energy to perturbed kinetic energy through the rising (sinking) motion of warm (cold) air parcels. KZ represents the generation (destruction) of KE by local convergence (divergence) of the perturbed geopotential flux. The last term KR denotes the net generation or dissipation of eddy kinetic energy by frictional, feedback from sub-seasonal eddies and other subgrid-scale effects. Following Lau and Lau (1992), we set the term KR as the opposite sign of the sum of CK, KA, KP and KZ to make the time-rate of change of KE to zero.

The distributions of the CK, KA, KP, KZ and KR at 850 hPa are shown in Fig. 3. The CK is the same as that in Fig. 2b with notable positive value in the confluence zone (shown by rectangle region in Fig. 3a). The KA is negative (positive) in the south (north) part of the confluent zone (Fig. 3b), likely caused by the northward advection of KE by climatological southwesterly monsoons. The KP is broadly positive in the TIO but negative in the Indo-Northwest Pacific at 850 hPa. The negative KP over the Indo-Northwest Pacific should be caused by the sinking motion of warm air parcel associated with the AAC pattern (Fig. 1). The KZ is positive in most regions from the Bay of Bengal to the NWP except in the east part of the confluent zone. In the lower troposphere, the KZ is dominated by the advection of perturbed geopotential height by cross-isobaric component of the horizontal wind perturbations $(-u'\frac{\partial\Phi'}{\partial x}-v'\frac{\partial\Phi'}{\partial y})$, so it tends to be positive value in the lower troposphere (Lau and Lau 1992). This cross-isobaric flow results in an increase of KE at the expense of the eddy geopotential energy in the lower troposphere. The KA and KZ terms mainly describe the redistribution of energy from one location to another, and the two terms should be not considered as real sources or sinks. The sum of CK, KA, KP and KZ is prominently positive from the NIO to the NWP, which supplies kinetic energy to the AAC pattern. The KR is negative in almost everywhere indicating its damping effect. The area-mean CK, KA, KP and KZ over the zonal confluence zone $(5^{\circ}-20^{\circ}N,$ $90^{\circ}-150^{\circ}E$) are $0.68 \times 10^{-6} \text{ m}^{-2} \text{ s}^{-3}$, $-0.06 \times 10^{-6} \text{ m}^{-2} \text{ s}^{-3}$, $-0.44 \times 10^{-6} \,\mathrm{m}^{-2} \,\mathrm{s}^{-3}$, and $1.4 \times 10^{-6} \,\mathrm{m}^{-2} \,\mathrm{s}^{-3}$, respectively,



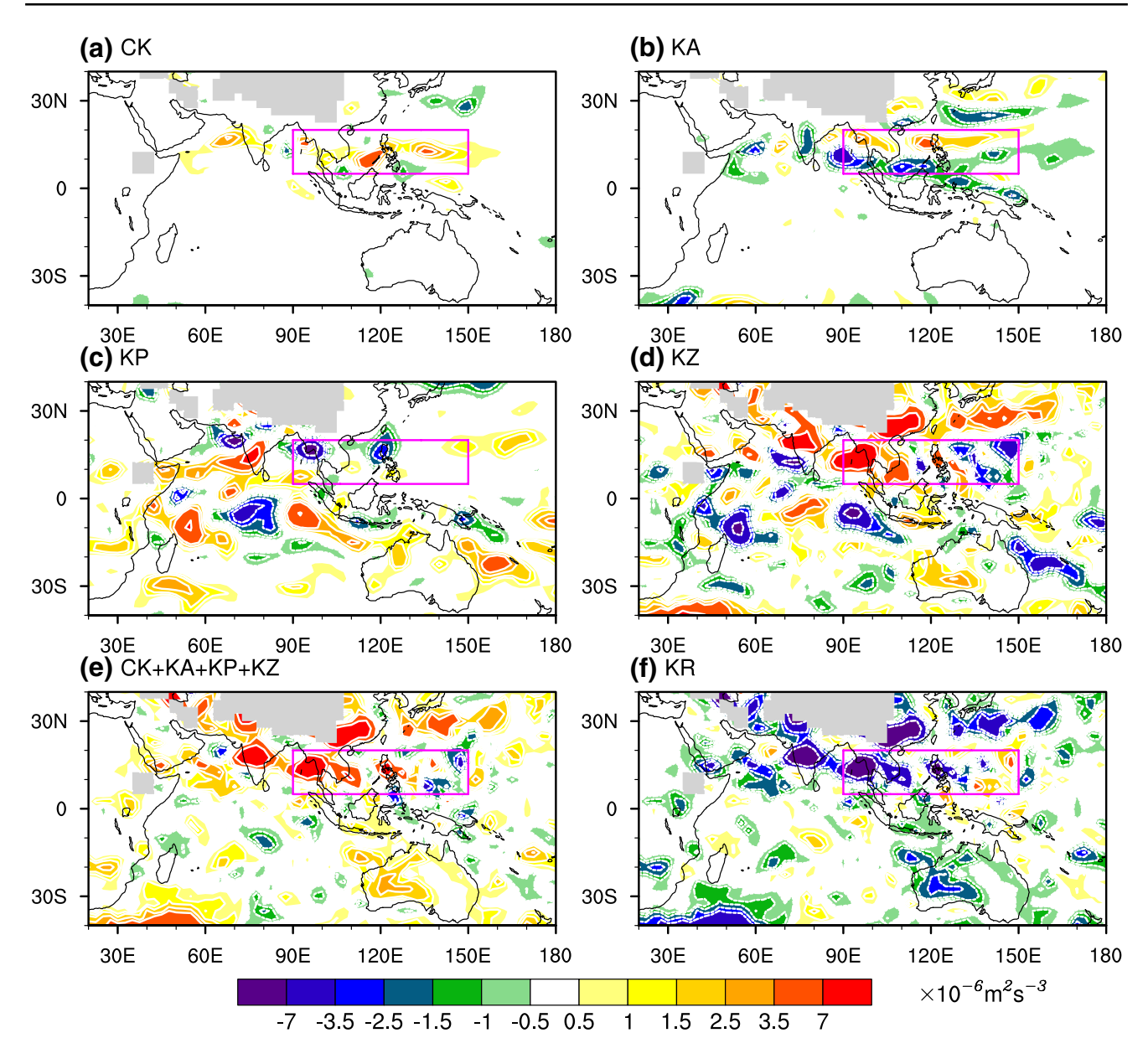


Fig. 3 The 850 hPa horizontal distributions of CK (a), KA (b), KP(c), KZ (d), their sum (e) and KR (f) for the atmospheric perturbations in post-El Niño summers. Each term is described in the Eq. (4)

and their total is 1.59×10^{-6} m⁻² s⁻³. Thus, the 850 hPa disturbed kinetic energy of the AAC pattern in the confluent zone is mostly contributed by *CK* and *KZ*. Since *KZ* does not explicitly depend on the background state, it cannot determine where the perturbations can grow fast. Thus, although the value of *KZ* is larger than *CK* in the confluence zone, the preferable location of AAC is mainly determined by *CK*.

Figure 4 shows the latitude-height section of zonally averaged (110°–150°E) CK, KA, KP, KZ and KR associated with the AAC in post-El Niño summers. The maximum positive CK, above 1.5×10^{-6} m⁻² s⁻³, is distributed from 5° to 20°N in the lower troposphere below 700 hPa,

in agreement with the confluent time-mean flow there. The KA shows a negative-positive-negative structure from 5° to 20° N in the lower troposphere, consistent with northward advection of perturbed kinetic energy by southwest monsoons. The KP is weak in the lower levels below 700 hPa while features a prominent negative-positive-negative structure from the equator to 25° N in the upper levels above 700 hPa. The positive KP from 5° to 12° N should result from the rising of warm air (not shown), while the negative KP from 10° to 25° N should be caused by the sinking of warm air. It is noticed that the vertical section of KP over the AAC is different from that



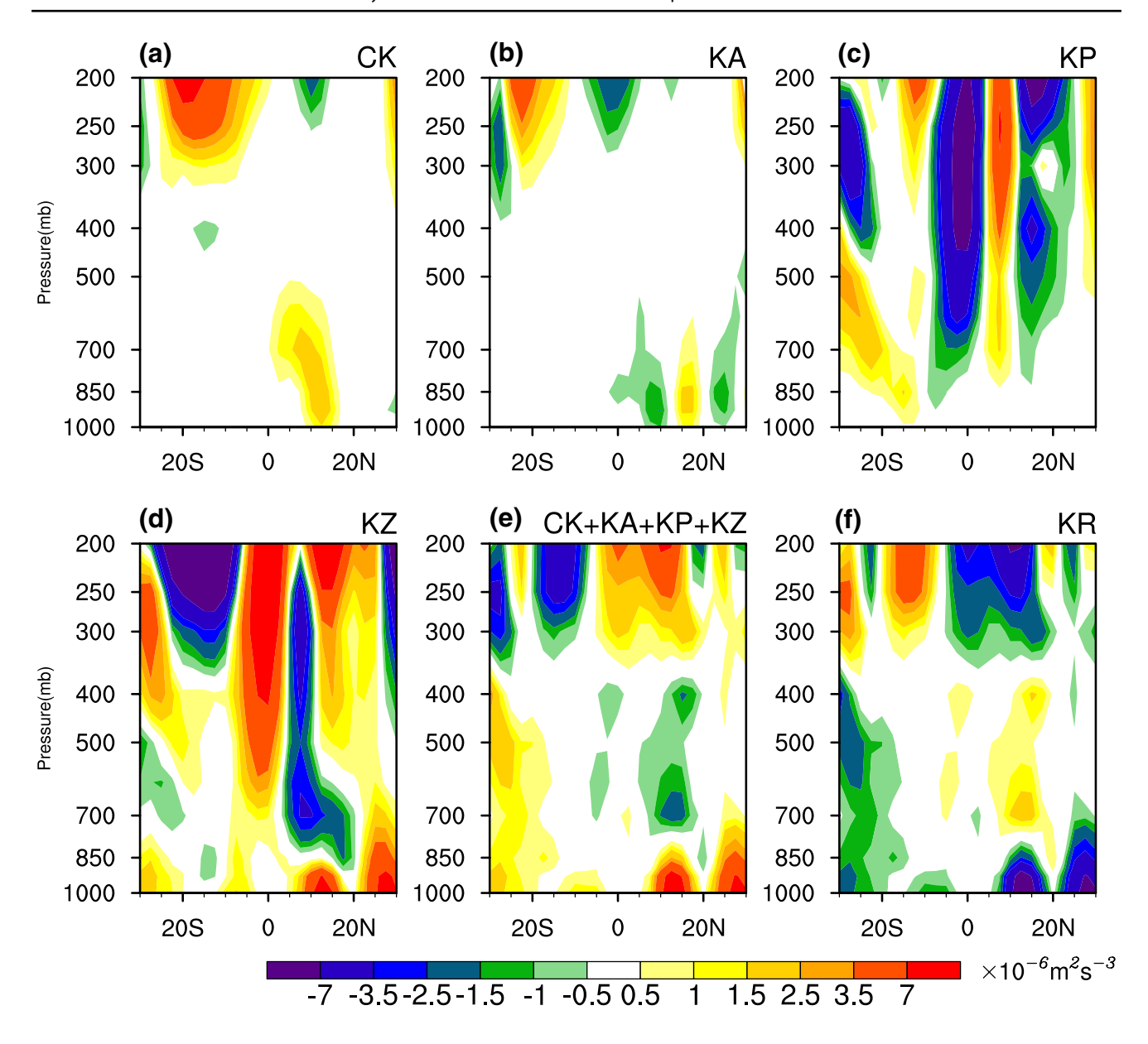


Fig. 4 Latitude-height section of $110^{\circ}-150^{\circ}$ E averaged CK (a), KA (b), KP(c), KZ (d), their sum (e) and KR (f) for the atmospheric perturbations in post-El Niño summers. Each term is descripted in the Eq. (4)

associated with the transient eddies over the NWP shown by Lau and Lau (1992). Associated with transient eddies, the rising (sinking) motions are generally accompanied by warm (cold) air parcel; thus, the *KP* is coherent positive. By contrast, the sinking motion on the south part of the AAC (from 12° to 25°N) is accompanied by warm air (Fig. 1), so the *KP* for the AAC pattern is dominated by negative values, indicating that transient eddies and the AAC pattern in the NWP are generated by different processes. The *KP* associated with transient eddies is mainly caused by the local diabatic heating (Lau and Lau 1992). While in the AAC pattern, the positive air temperature anomalies over the NWP are partly caused by remote

oceans (Xie et al. 2009). Thus, the *KP* in this case is not totally governed by the local diabatic heating. As shown in the Eq. (4), the *KZ* can be divided into three terms, and the last term $(-\omega' \frac{\partial \Phi'}{\partial P})$ is equal to -KP; thus, the *KP* in the middle and upper troposphere is offset by the *KZ* (Fig. 4c, d). In the lower levels, the *KZ* is dominated by $-u' \frac{\partial \Phi'}{\partial x} - v' \frac{\partial \Phi'}{\partial y}$, and the cross-isobaric flow could increase *KE* at the expense of the eddy geopotential energy. From 5° to 12°N, the *KZ* term is positive below 800 hPa but negative in the upper levels, suggesting it acts to redistribute the *KE* from the upper and middle troposphere, generated by *KP*, to the lower levels. The sum of *CK*, *KA*, *KP*



and KZ is positive in the lower troposphere (Fig. 4e), which could help the AAC pattern counter damping (shown in Fig. 4f).

Figure 5 shows the vertical integral (from 1000 to 200 hPa) of local baroclinic energy conversion *CP*, defined as

$$CP = \left[-\frac{f}{\sigma} v' T' \frac{\partial u_b}{\partial P} + \frac{f}{\sigma} u' T' \frac{\partial v_b}{\partial P} \right],\tag{5}$$

where f the Coriolis parameter, $\sigma = (R\bar{T}/C_p p) - d\bar{T}/dp$, and the other variables are the same as the Eq. (4). The square bracket denotes a vertical integral that was taken from the 1000 to the 200 hPa level. In the Indo-Northwest Pacific, the CP is dominated by negative value. In summer, the Asian continent is a warm center (contours in Fig. 5), and the meridional gradient $(\frac{\partial T}{\partial y})$ and the zonal gradient $(\frac{\partial T}{\partial x})$ of mean air temperature over the Indo-Northwest Pacific are generally positive and negative, respectively. As shown in Fig. 1, the AAC-related v'T' and u'T' are respectively positive and negative; so, both of them act to enhance the summer climatological temperature gradient. Consequently, the baroclinic conversion from the mean state to the AAC pattern is negative over the Indo-Northwest Pacific, indicating that the CP act to damp the AAC pattern.

The energetics analyses indicate that the ACC pattern can gain kinetic energy in the lower troposphere. In detail, perturbed kinetic energy of the AAC pattern is mostly contributed by the term of *CK* and *KZ*. The result confirms that the conversion of local kinetic energy from the basic state in the confluence zone in the Indo-Northwest Pacific favors the developing of the AAC.

b. LBM experiments

To test the dependency of the AAC on the summer atmospheric basic state over the Indo-Northwest Pacific, we conduct two LBM experiments: EXP1 and EXP2, forced by the same heating over the TIO but with different basic states. Figure 6a, b show the prescribed heat source imposed in model. In the horizontal, the heating has a cosine-squared pattern (Fig. 6a). This vertical profile of the heating peaks at 0.45 sigma level (about 450-hPa) with 1 K day⁻¹. The heating structure and magnitude is comparable to that of Xie et al. (2009). The TIO heat source mimics the effect of positive SST and rainfall anomalies in post-El Niño summers. The EXP1 uses the observed JJA-mean climatological basic state from 1979 to 2016 (Fig. 6c), while the EXP2 uses a basic state with the confluence zone over the Indo-Northwest Pacific having been artificially removed (Fig. 6d). The basic state in EXP2 is computed by the following procedure. From only 70°E to 170°E replace the basic state to the zonal mean of that in EXP1 from only 60°E to 180°. Then at the western and eastern boundaries, within 50°E to 70°E and 170°E to 170°W, let values linearly transition from the EXP1 60°E to

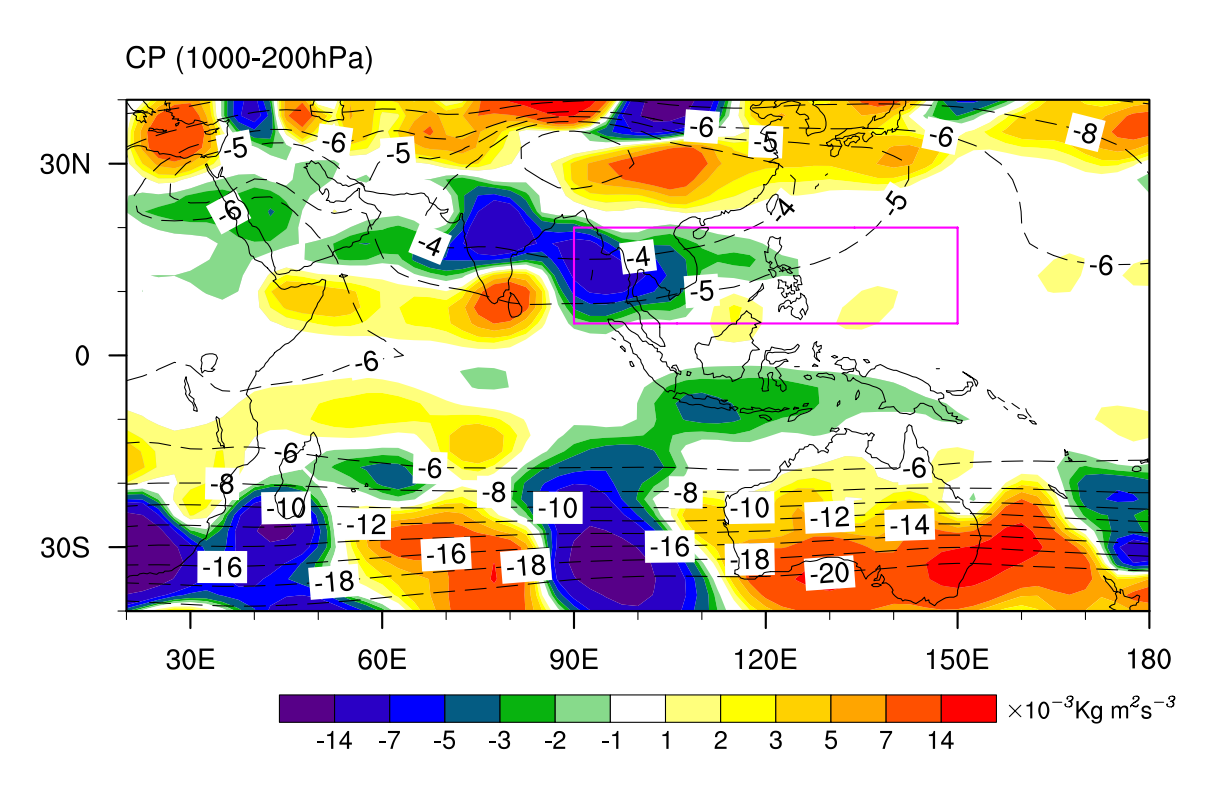


Fig. 5 Vertically integrated baroclinic energy conversion (*CP* in the Eq. (5); colors), superimposed on the JJA climatological mean temperature at the 500 hPa level (contours, °C)



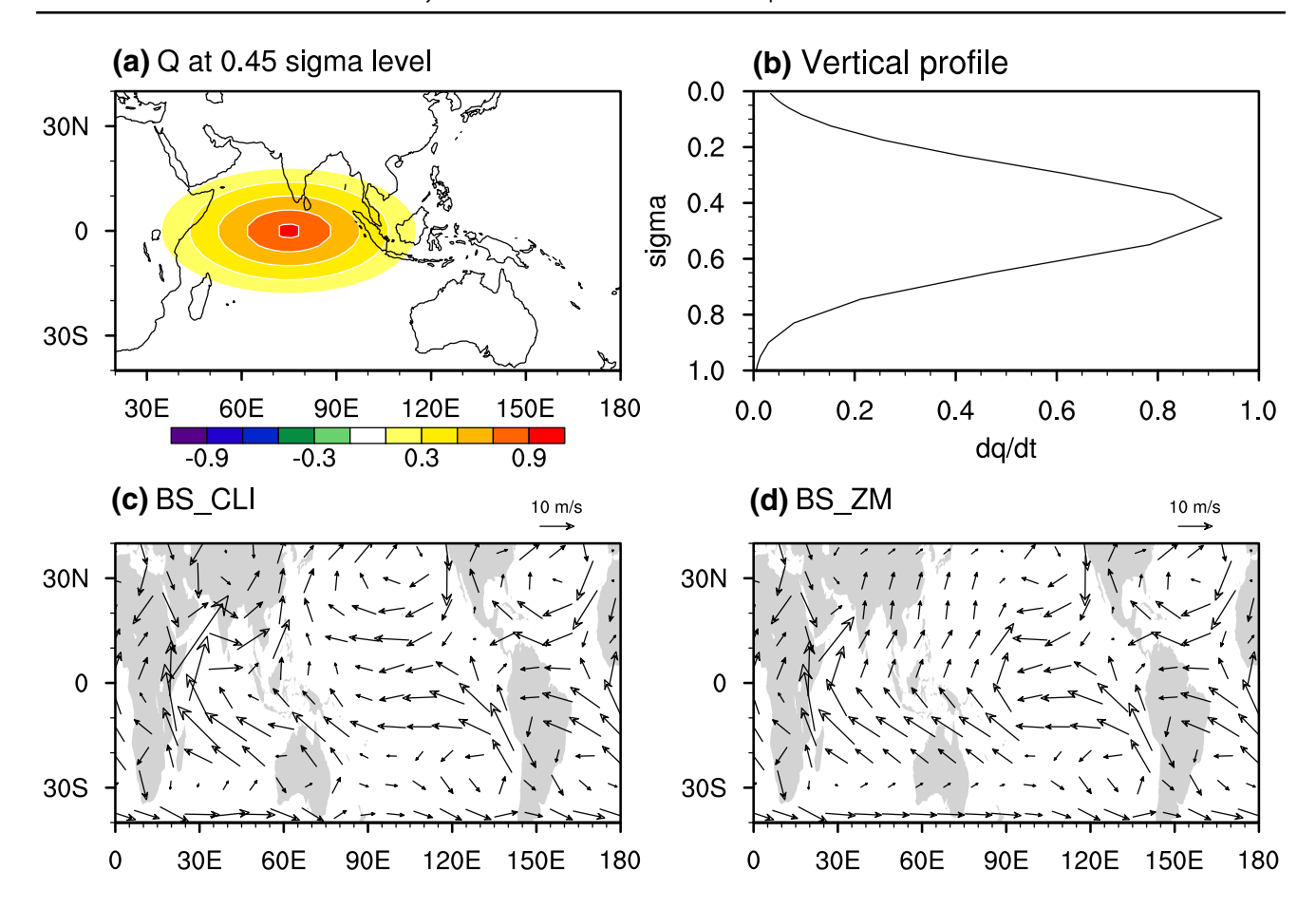


Fig. 6 Horizontal (**a**) and vertical (**b**) distribution of atmospheric diabatic heating over the TIO (K day⁻¹) for both LBM EXP1 and EXP2. The basic state horizontal wind structures (vectors) at 0.94995 sigma

level in LBM EXP1 (c) and EXP2 (d). In the EXP2, the confluence zone over the Indo-Northwest Pacific is removed

180° zonal mean to those averaged between 50°E–60°E and 180°–170°W, respectively. Outside of these use equivalent values to those in EXP1.

Figure 7 compares results from two experiments forced by the same TIO heating but under different background states. In EXP1, there are strong easterly wind response at 850-hPa over the Indo-Northwest Pacific extending from the International Date Line to the Arabian Sea together with an anomalous cyclone in the Arabian Sea (Fig. 7a). Although the heating is symmetric about the equator, the low-level wind responses are highly asymmetric, with a stronger response north than south of the equator. The wind response pattern in EXP1 is similar to that in the observations in post-El Niño summers in the tropical region (Fig. 1a). The major difference is that the anticyclonic circulation north of the easterly winds anomalies is not clear in EXP1. This is likely due to the absence of moist processes in the dry model. Compared to EXP1, the easterly responses over the Indo-Northwest Pacific in EXP2 are much weaker (Fig. 7b). Since the confluence zone over the Indo-Northwest Pacific is removed in EXP2, the CK at 850 hPa in EXP2 is much weaker than that in EXP1 (Fig. 7a, b), which likely results in weaker easterly responses over the Indo-Northwest Pacific in EXP2 than in EXP1.

Figure 7c shows the latitude-height section of 90°–150°E averaged air temperature and zonal wind responses in LBM EXP1. In the tropics, there are easterly winds below 350hPa, westerly winds above 350-hPa, and maximum positive temperature responses around 350-hPa. The pattern broadly agrees with Gill's solution to symmetric heating (Gill 1980) and observations in post-El Niño summers (Fig. 1a). The air temperature and zonal wind responses are nearly symmetric about the equator in the middle and upper troposphere, but the zonal wind anomalies are much stronger north than south of the equator at the lower levels, consistent with observations (shown in Fig. 1b). In LBM EXP2 (Fig. 7d) with zonalmean basic state, the asymmetry in the lower-level zonal wind is much weaker than in EXP1. The simulated results confirm that zonal variations in the mean flow, specifically the confluence, enhance zonal wind anomalies over the Indo-Northwest Pacific, consistent with the energetics analysis.



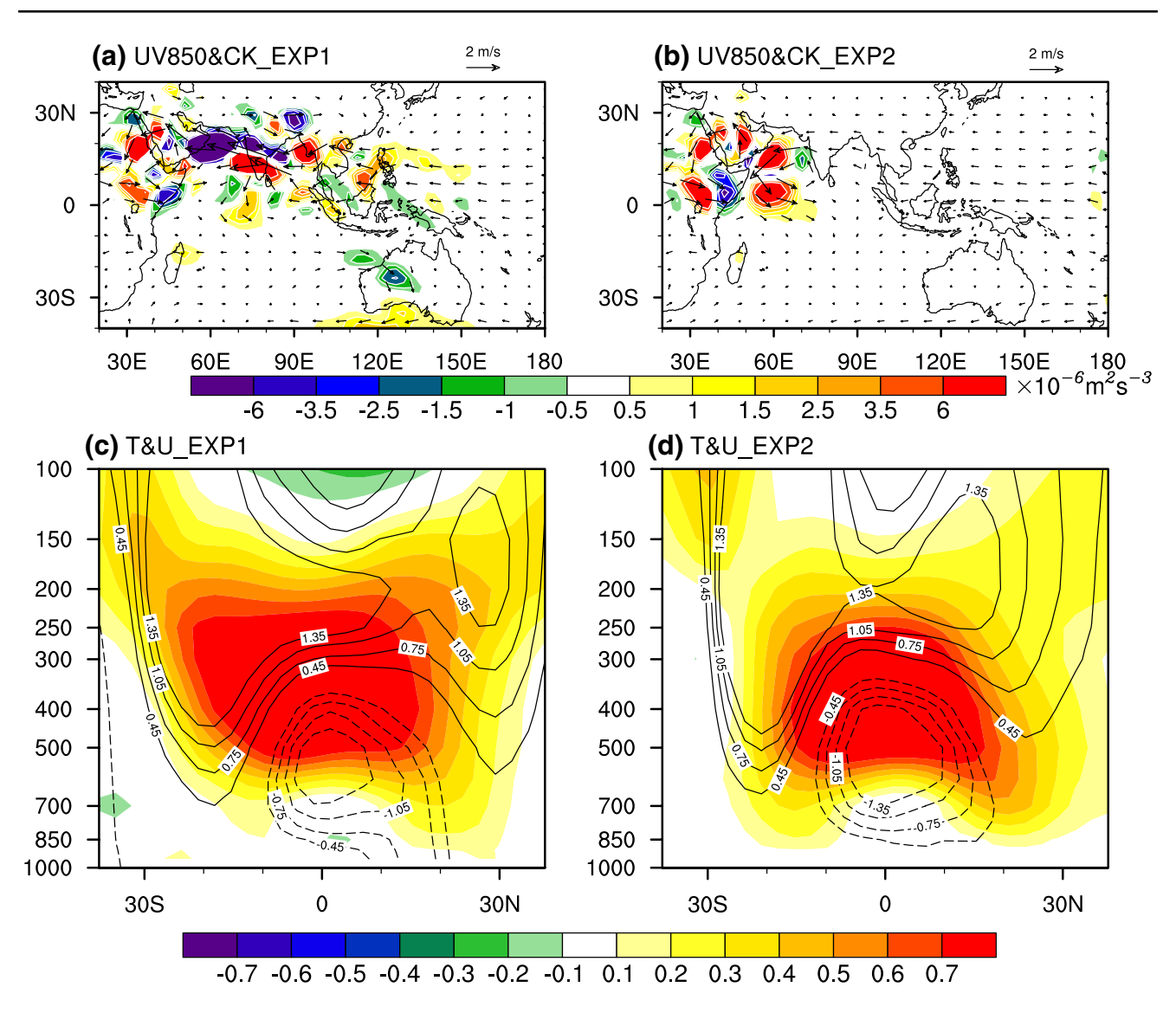


Fig. 7 The 850-hPa wind responses (vectors) and CK (colors) in LBM EXP1 (a) and EXP2 (b). Latitude-height section of $90^{\circ}-150^{\circ}E$ averaged zonal wind (contours, interval at 0.3 ms^{-1}) and air temperature (colors, K) anomalies in LBM EXP1 (c) and EXP2 (d)

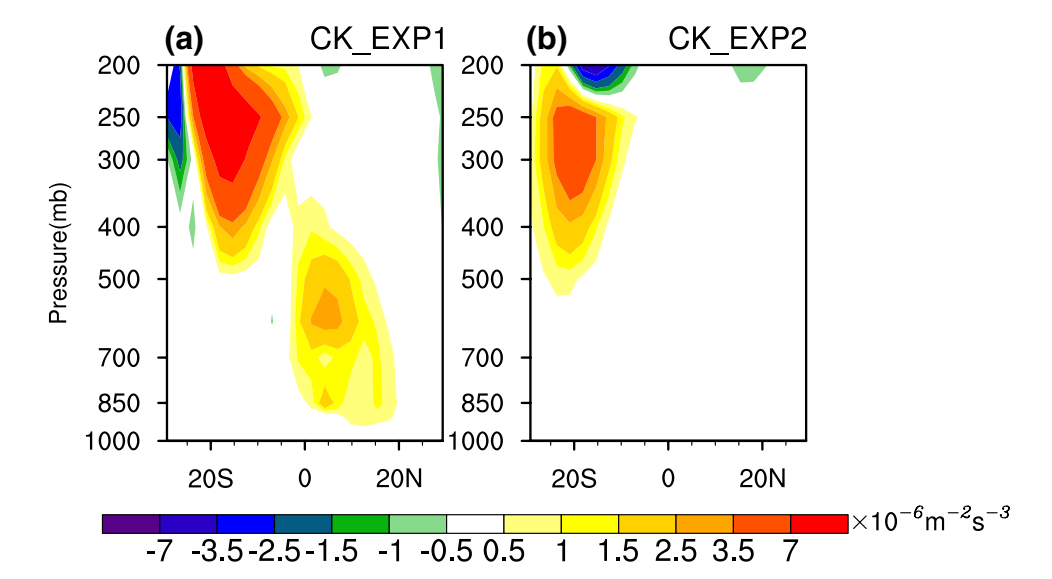
To understand why the response of low-level zonal wind in the Indo-Northwest Pacific is stronger in EXP1 than EXP2, we compare the CK of the two experiments. Figure 8a, b show the vertical cross section of zonally averaged $(110^{\circ}-150^{\circ}E)$ CK of the EXP1 and EXP2, respectively. The most striking difference exists in the lower troposphere north to the equator where the CK is significant positive in the EXP1 but very weak in the EXP2. The difference is due to the confluence zone over the Indo-Northwest Pacific is artificially removed in basic state of the EXP2, so the term CKx is reduced. The result indicates that the zonally elongated perturbations in the lower troposphere over the Indo-Northwest Pacific in EXP1 more easily obtained kinetic energy from the basic state than that in EXP2, so they are stronger in EXP1.

5 The moist feedback

This section further discusses how the easterly wind anomalies over the NWP help form the AAC pattern through moist feedback. Figure 9a shows the wind responses at 850-hPa (black arrows) and 1000-hPa (magenta arrows) in the LBM EXP1 experiment. At 850-hPa, easterly winds in the NWP at 850-hPa peak around 10°N. At 1000-hPa, surface friction turns the winds northeasterly, leading to surface divergence in the NWP and convergence in the equatorial region. In comparison, the easterly anomalies and their-induced surface divergence in the EXP2 is much weaker than the EXP1 (Fig. 9b). The observed wind anomalies at 850-hPa and 1000-hPa in El Niño decaying summer are shown in Fig. 9c. From the equator to 20°N, the wind structure at 850-hPa and 1000-hPa and the surface divergence in LBM EXP1



Fig. 8 Latitude-height section of 110°–150°E averaged *CK* in LBM EXP1 (a) and EXP2 (b)



resemble the observations. The easterly wind–induced divergence can suppress convection and lead to negative diabatic cooling in the atmosphere, which in turn favors the AAC developing (Xie et al. 2009; Hamouda and Kucharski 2019). The dry LBM mode does not include this moist process, so the anticyclonic circulation to the north of the easterly wind anomalies is weak in EXP1.

To test how this easterly wind-induced off-equatorial divergence aids the AAC pattern formation in the presence of moist process, we conduct an experiment (EXP3) with a supplementary negative heat source added over the NWP. For simplicity, the negative heating is prescribed in an elliptical region over the NWP (shown in Fig. 10), with the peak magnitude of -0.6 K day^{-1} at 0.45 sigma level. The location of the negative heat source is determined by the center of the easterly wind-induced divergence, and the magnitude of the negative heat source is comparable to the observed heating in post-El Niño summers (figure not shown). The structure of wind responses in the EXP3 resemble the observed AAC (Fig. 1a), with an anticyclone over the NWP and easterlies in 5°-20°N from the Arabian Sea to the International Date Line. The results indicate that there exists a moist feedback between atmospheric circulation and convective activities in the AAC formation. On one hand, enhanced easterly wind anomalies over the Indo-Northwest Pacific can lead to surface divergence in the subtropical NWP, which may suppress convective activities. On the other hand, the suppressed convective activities can trigger the AAC pattern and in turn enhance easterly wind over Indo-Northwest Pacific. As suggested by Xie et al. (2009), the moist feedback play an important role to enhance the AAC pattern. Some issues should also be noticed. The dry LBM experiments cannot simulate the detailed interactive processes between circulation and convection involved with the AAC, which deserved further study in the future.

The LBM results support our hypothesis involving the following adjustments: the TIO warming forces the Kelvin wave; the mean confluent flow in the Indo-Northwest Pacific amplifies the lower-level easterly wind anomalies via kinetic energy conversion; and the enhanced easterly winds anomalies lead to an AAC pattern over the NWP by inducing surface Ekman divergence.

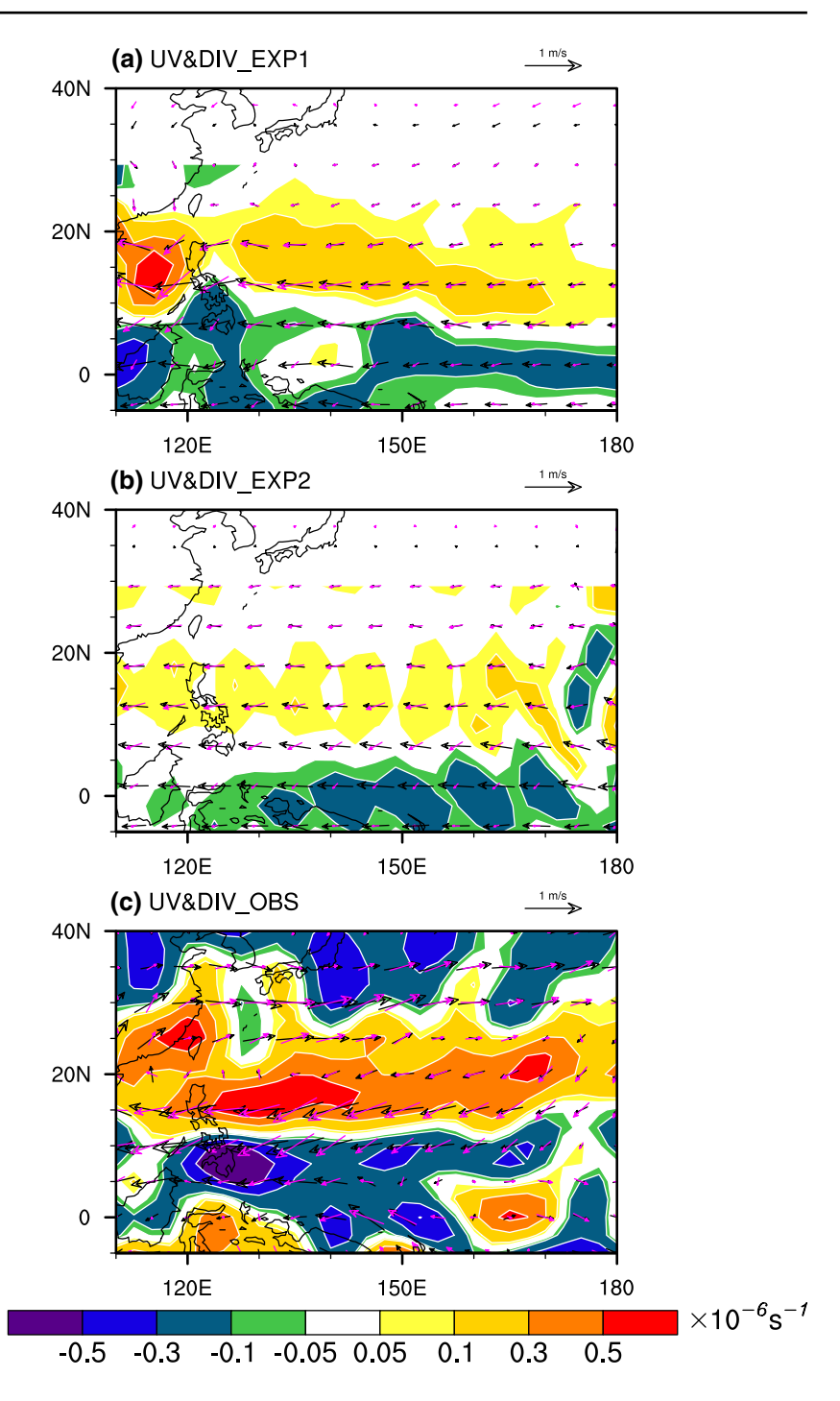
6 Optimal forcing for the AAC pattern

This section is to investigate what kind of atmospheric forcing is most effective in exciting the AAC pattern. We divide the region from 35°S to 35°N into 96 box regions, each 10° latitude $\times 30^{\circ}$ longitude. In each box region, we impose a heat source. The heat source has a cosine elliptical pattern, with a peak of 1 K day⁻¹ at 0.45 sigma level in the vertical. The horizontal distributions and vertical profile of the heat source are shown in Fig. 11. We obtain the steady linear response by time-integrating LBM. The 96-member responses to each localized heating together constitute an ensemble. We can test the relative contribution of each localized heating to the AAC based on the ensemble. The method is similar to the so-called Green's function approach introduced by Branstator (1985), who showed that the general solutions to a linear system are simply integrals of the Green's function weighted by the forcing distribution.

We perform an empirical orthogonal function (EOF) analysis on the 96 zonal wind responses at 850-hPa over the Indo-Northwestern Pacific (5°–20°N, 90°–150°E) in the ensemble simulations. The two leading EOF modes explain 46% and 30%, respectively, well separate by the criterion of North et al. (1982). Figure 12a, b show the regression of 850-hPa winds onto the first and the second principle components (PC1 and PC2), respectively. For



Fig. 9 The wind anomalies at 850-hPa (black vectors) and 1000-hPa (magenta vectors) and the divergence (colors) at 1000-hPa in the LBM EXP1 (a) and EXP2 (b). c is the same as a but for the observed regression of JJA winds onto the preceding NDJ Niño3.4 SST index from 1979 to 2016



simplicity, we use the regressions of winds onto PC1 and PC2 to represent the first and second leading EOF (EOF1 and EOF2) modes. The EOF1 mode (Fig. 12a) mainly features an AAC pattern over the NWP and anomalous easterly winds on the south flank extending from the International Date Line to the Arabian Sea. The EOF1 mode resembles the observed AAC pattern in post-El Niño decaying summers. The EOF2 mode (Fig. 12b) displays easterly wind anomalies over the TIO and western Pacific and enhanced southwest monsoon from the NIO to East

Asia. As only the EOF1 mode is related to the AAC pattern, we mainly focus on the EOF1 mode. Even analyzing on a larger domain such as 10°S-25°N, 50°-150°E, the same EOF1 pattern is reproduced, suggesting it is not sensitive to domain selection.

Since the EOF1 mode is similar to the AAC pattern, PC1 could represent the contribution of each heat source to the AAC pattern. Figure 13a shows PC1 in terms of the geographic location of the heat sources. The maximum positive values are distributed in the TIO, while negative values in



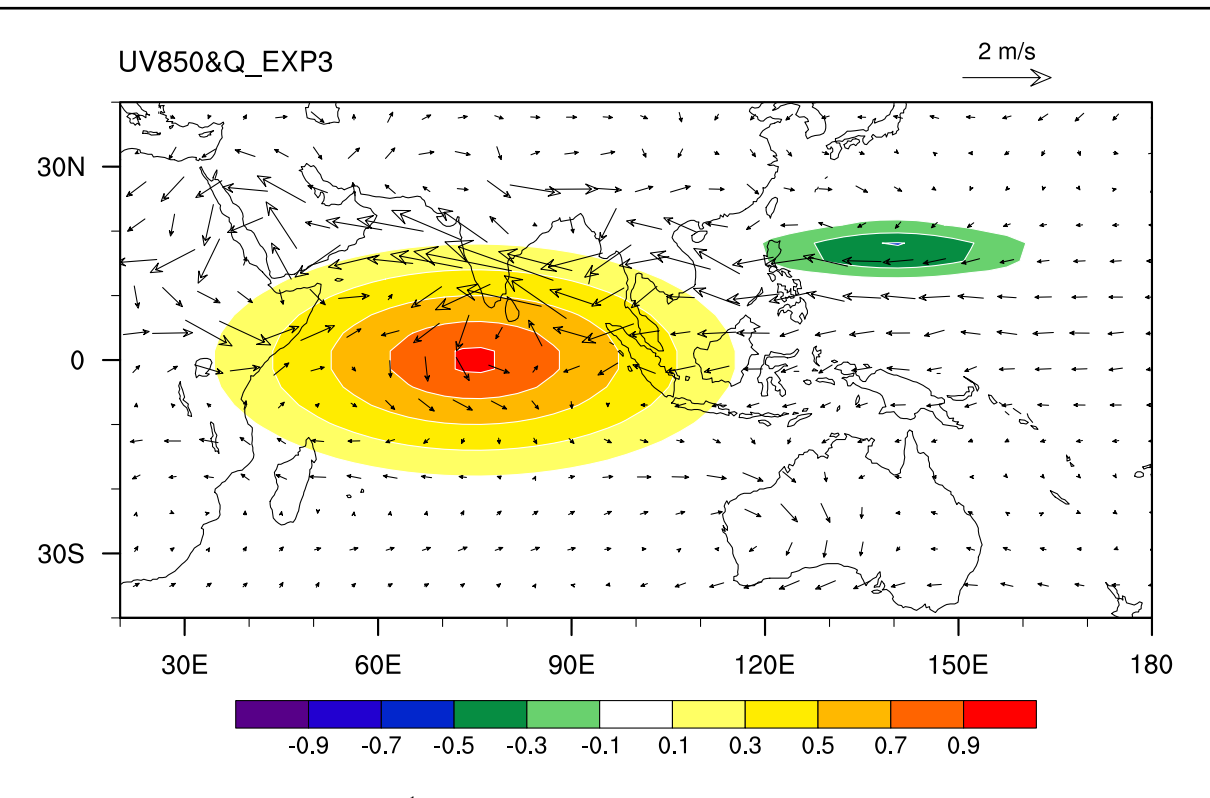


Fig. 10 The 850-hPa wind response (vectors, ms^{-1}) to positive atmospheric heating over the TIO and negative heating over the NWP (colors, K day⁻¹) in LBM EXP3 with the observed JJA-mean basic state

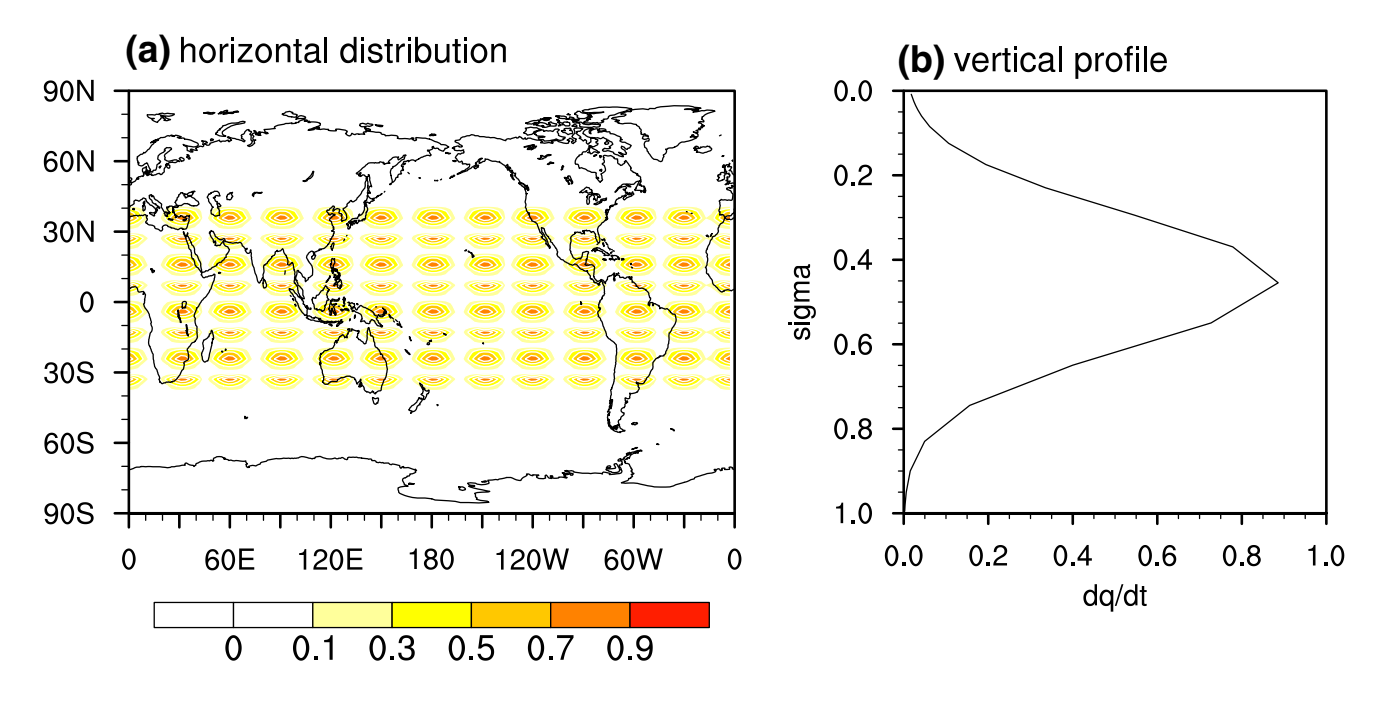
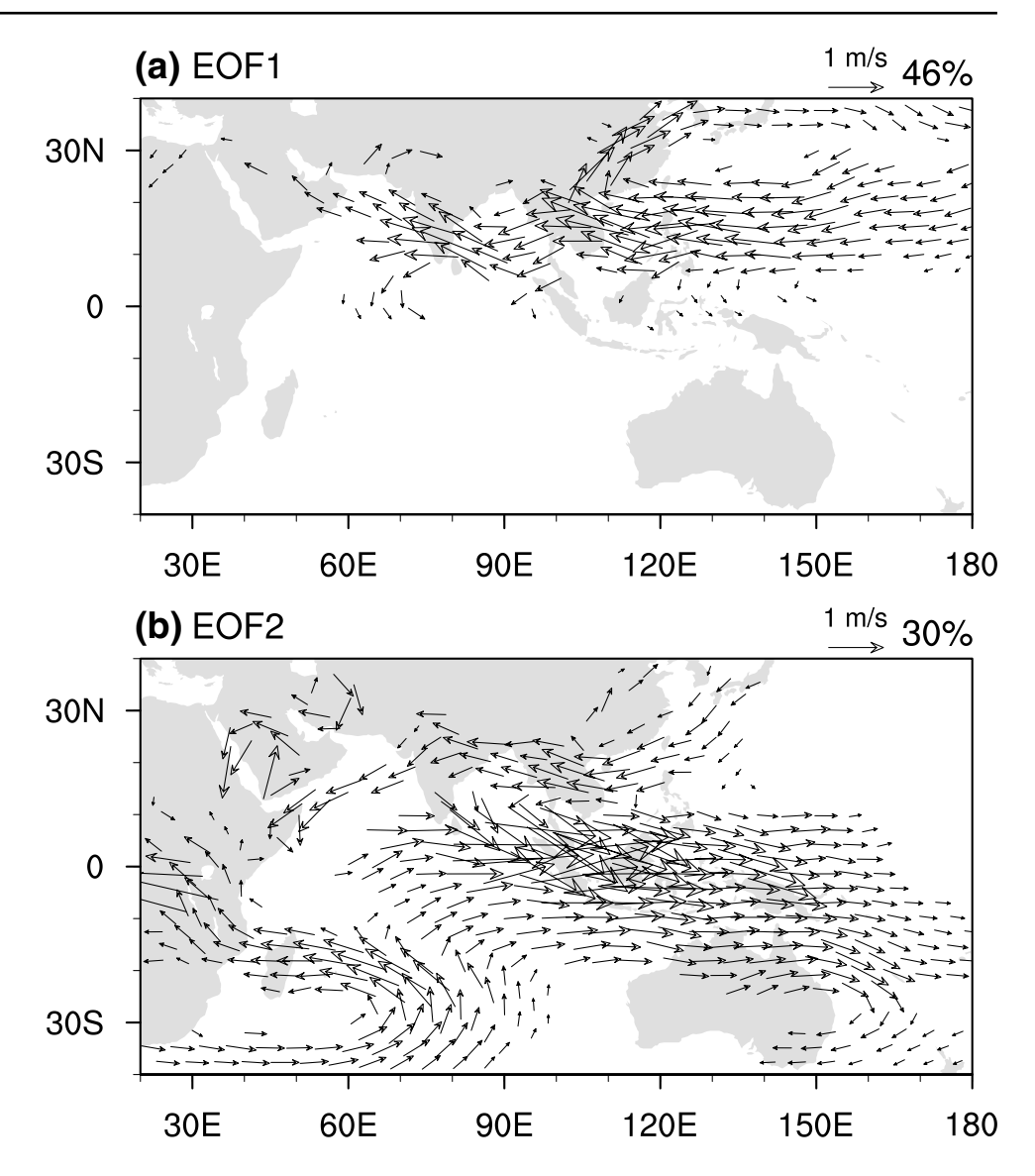


Fig. 11 The horizontal distribution (a) and vertical profile (b) of heating of the 96-member simulations in the LBM Green's function. For simplicity, the 96 members of heating are shown in one map

the subtropical NWP. The magnitude of negative values in the subtropical NWP is slightly larger than the magnitude of positive value in the TIO, suggesting that the AAC pattern is more efficiently forced by local forcing. Thus, the optimal forcing for EOF1 is diabatic heating over the TIO and cooling over the NWP. We also calculate the area-mean



Fig. 12 The regressions of 850-mb winds (arrows, ms⁻¹) onto the two leading PCs of 96-member LBM simulation. The EOF analysis is performed over the Indo-Northwestern Pacific (5°-20°N, 90°-150°E). The first and the second mode explain 46% and 30% of the variance, respectively. Only the anomalous winds exceeding the 95% confidence level are shown



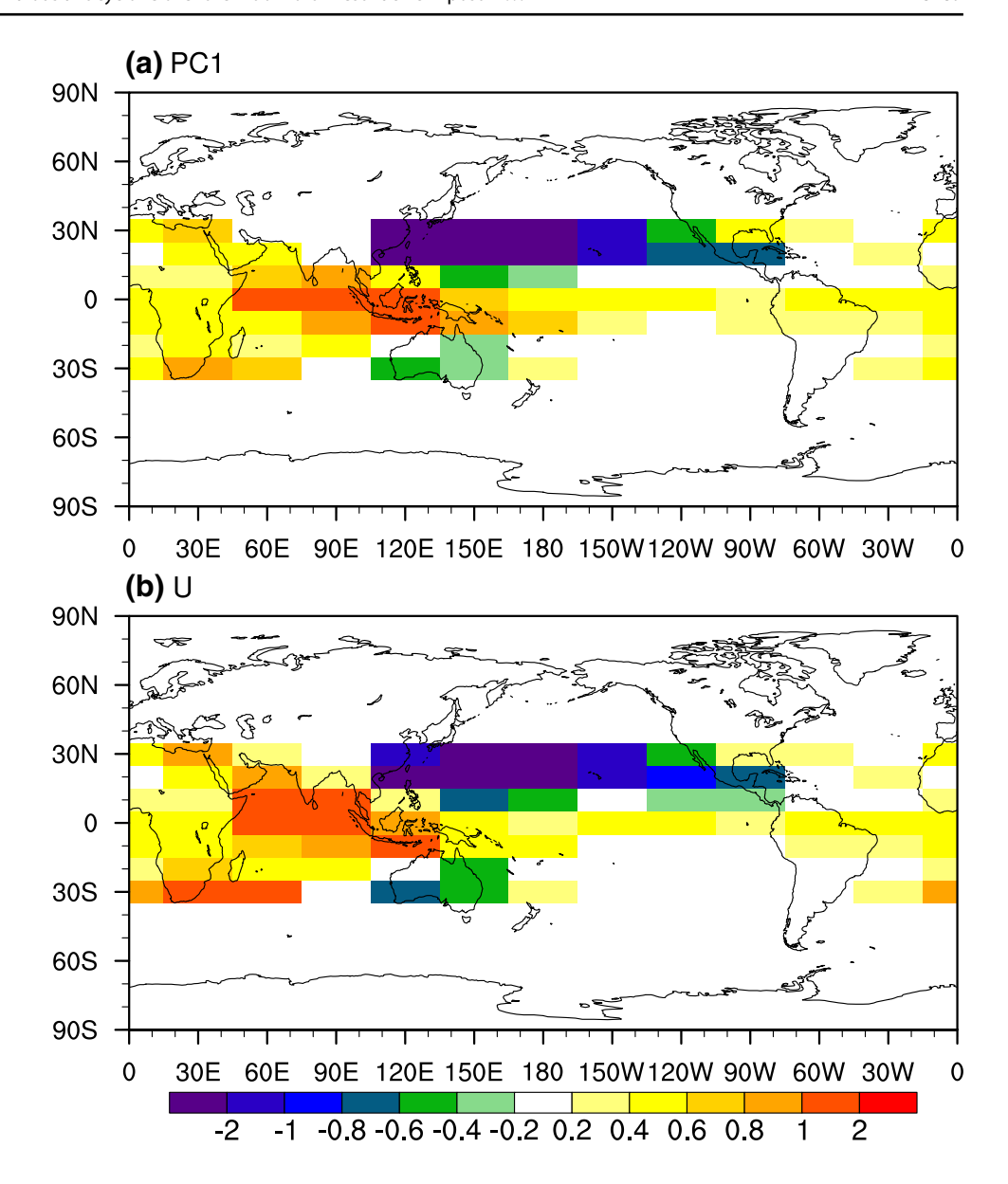
zonal wind over the Indo-Northwest Pacific (5°-20°N, 70°-150°E) in each response of the 96-member LBM's simulations. Figure 13b show the area-mean zonal winds in horizontal distribution of heat sources, which represents the heating contribution to the easterly wind anomalies over the Indo-Northwest Pacific. The pattern is very similar to that in PC1, indicating that the combination of atmospheric heating over the TIO and cooling over the NWP is effective in forcing the AAC or the easterly wind anomalies over the Indo-Northwest Pacific. The pattern of the optimal forcing is consistent with the previous results that the formation of AAC is linked with SST warming in the TIO (Xie et al. 2009) and cooling in the NWP (Wang et al. 2003; Fan et al. 2013; Xiang et al. 2013; Jiang et al. 2017). A similar Green function analysis was performed by Hirota and Takahashi (2012) who calculated a number of linear responses to external forcing distributed homogeneously over the Northern Hemisphere. The dominant atmospheric mode of their homogenous forcing experiment features a tripolar pattern from the Philippines to the East Siberia. The tripolar pattern includes an AAC over the subtropical NWP. Their result shows that the AAC pattern over the subtropical NWP, as a part of the tripolar pattern, can be thought of as an atmospheric internal mode.

7 Summary and discussion

We have investigated the effect of the basic flow over the Indo-Northwest Pacific on interannual variability in atmospheric circulation by diagnostic and experimental approaches. We show that the mean flow over the



Fig. 13 a The normalized PC1 (colors) of the 96-member LBM's simulation in horizontal distribution of heat sources. **b** is the same as **a** but for the areamean zonal wind at 850-hPa over the Indo-Northwest Pacific (5°-20°N, 90°-150°E)



Indo-Northwest Pacific promotes to anchor the AAC. Specifically, the climatological confluence zone acts to amplify the TIO warming-induced easterly wind anomalies via kinetic energy conversion from the mean flow. The enhanced easterly wind anomalies in turn induce Ekman divergence at the surface over the off-equatorial NWP and trigger an AAC pattern through moist feedback. Circulation-convective feedback and the mean flow structure are both important in creating the preferred AAC pattern.

We use a method similar to the Green's function approach to determine the structure of the optimal thermal forcing for the AAC pattern. Positive diabatic heating over the TIO and negative heating over the NWP prove to be effective in exciting the AAC pattern. The result is broadly consistent with observational analyses that SST cooling in the NWP (Wang et al. 2003; Fan et al. 2013; Xiang et al. 2013; Jiang

et al. 2017) and the SST warming in the TIO (Yang et al. 2007; Li et al. 2008; Xie et al. 2009; Chowdary et al. 2010) significantly contribute to the development of an AAC.

The ENSO effect on the AAC displays considerable interdecadal modulations. In recent decades, El Niño induces significant warming and positive rainfall anomalies in the TIO, a pattern that could trigger the AAC (Wang et al. 2008; Huang et al. 2010; Xie et al. 2010). However, El Niño's teleconnection to SST in other basins may vary on interdecadal time scale (Huang et al. 2010; Chowdary et al. 2012) and under global warming (Hu et al. 2014; Jiang et al. 2018; He et al. 2019). For example, the El Niño-induced TIO-warming could not persist into boreal summer during 1948–1976, following a weakening in the impact of El Niño on AAC (Xie et al. 2010; Huang et al. 2010). In addition to ENSO, other tropical variability such as the Indian Ocean dipole (Guan



and Yamagata 2003) and Atlantic SST anomalies (Rong et al. 2010) may also contribute to the AAC development. Our results likely suggest that any external forcing that leads to a similar heating structure as the optimal thermal forcing pattern could lead to an AAC anomaly. This result may help us to better understand the relationship between AAC and tropical air—sea couple modes, as well as improved prediction of the AAC and its associated climate anomalies.

Acknowledgements The study is jointly supported by the Strategic Priority Research Program of Chinese Academy of Sciences (XDA20060502), the National Natural Science Foundation of China (41425086, 41661144016, and 41706026), U.S. National Science Foundation (1637450), and State Key Laboratory of Tropical Oceanography, South China Sea Institute of Oceanology, Chinese Academy of Sciences (project no. LTO1704).

Compliance with ethical standards

Conflict of interest The authors declare no competing interests.

References

- Adler RF, Huffman GJ, Chang AE, Ferraro RR, Xie P, Janowiak JE, Rudolf B, Schneider U, Curtis S, Bolvin D (2003) The version-2 global precipitation climatology project (GPCP) monthly precipitation analysis (1979—present). J Hydrometeorol 4(6):1147–1167
- Branstator G (1985) Analysis of general circulation model sea–surface temperature anomaly simulations using a linear model. Part I: forced solutions. J Atmos Sci 42(21):2225–2241
- Branstator G (1990) Low-frequency patterns induced by stationary waves. J Atmos Sci 47(5):629–649
- Chang CP, Zhang YS, Li T (2000) Interannual and interdecadal variations of the East Asian summer monsoon and tropical Pacific SSTs. Part I: roles of the subtropical ridge. J Clim 13(24):4310–4325
- Chowdary JS, Xie S-P, Lee J-Y, Kosaka Y, Wang B (2010) Predictability of summer northwest Pacific climate in 11 coupled model hindcasts: local and remote forcing. J Geophys Res Atmos 115:D22121
- Chowdary JS, Xie SP, Tokinaga H, Okumura YM, Kubota H, Johnson N, Zheng XT (2012) Interdecadal variations in ENSO teleconnection to the Indo–Western Pacific for 1870–2007. J Clim 25(5):1722–1744
- Chowdary JS, Harsha HS, Gnanaseelan C, Srinivas G, Parekh A, Pillai P, Naidu CV (2017) Indian summer monsoon rainfall variability in response to differences in the decay phase of El Niño. Clim Dyn 48(7):2707–2727
- Fan L, Shin SI, Liu QY, Liu ZY (2013) Relative importance of tropical SST anomalies in forcing East Asian summer monsoon circulation. Geophys Res Lett 40(10):2471–2477
- Fu C, Ye D (1988) The tropical very low-frequency oscillation on interannual scale. Adv Atmos Sci 5(3):369–388
- Gill AE (1980) Some simple solutions for heat-induced tropical circulation. Q J R Meteorol Soc 106(449):447–462
- Guan Z, Yamagata T (2003) The unusual summer of 1994 in East Asia: IOD teleconnections. Geophys Res Lett 30(10):51
- Hamouda ME, Kucharski F (2019) Ekman pumping mechanism driving precipitation anomalies in response to equatorial heating. Clim Dyn 52(1):697–711

- He C, Zhou TJ, Li T (2019) Weakened anomalous Western North Pacific anticyclone during an El Nino-decaying summer under a warmer climate: dominant role of the weakened impact of the tropical Indian Ocean on the atmosphere. J Clim 32(1):213–230
- Hirota N, Takahashi M (2012) A tripolar pattern as an internal mode of the East Asian summer monsoon. Clim Dyn 39(9):2219–2238
- Hu K, Huang G, Huang R (2011) The impact of tropical Indian Ocean variability on summer surface air temperature in China. J Clim 24(20):5365–5377
- Hu K, Huang G, Qu X, Huang R (2012) The impact of Indian Ocean variability on high temperature extremes across south of Yangtze River valley in late summer. Adv Atmos Sci 29(1):91–100
- Hu K, Huang G, Zheng X-T, Xie S-P, Qu X, Du Y, Liu L (2014) Interdecadal variations in ENSO influences on Northwest Pacific–East Asian early summertime climate simulated in CMIP5 models. J Clim 27(15):5982–5998
- Hu K, Xie S-P, Huang G (2017) Orographically anchored El Niño effect on summer rainfall in Central China. J Clim 30(24):10037–10045
- Huang G, Hu K, Xie S-P (2010) Strengthening of tropical Indian Ocean teleconnection to the Northwest Pacific since the Mid-1970s: an atmospheric GCM study. J Clim 23(19):5294–5304
- Jiang W, Huang G, Hu K, Wu R, Gong H, Chen X, Tao W (2017) Diverse relationship between ENSO and the Northwest Pacific summer climate among CMIP5 models: dependence on the ENSO decay pace. J Clim 30(1):109–127
- Jiang W, Huang G, Huang P, Hu K (2018) Weakening of Northwest Pacific anticyclone anomalies during post–El Niño summers under global warming. J Clim 31(9):3539–3555
- Kanamitsu M, Ebisuzaki W, Woollen J, Yang SK, Hnilo J, Fiorino M, Potter G (2002) Ncep–doe amip-ii reanalysis (r-2). Bull Am Meteorol Soc 83(11):1631–1644
- Klein SA, Soden BJ, Lau N-C (1999) Remote sea surface temperature variations during ENSO: evidence for a tropical atmospheric bridge. J Clim 12(4):917–932
- Kosaka Y, Nakamura H (2006) Structure and dynamics of the summertime Pacific–Japan teleconnection pattern. Q J R Meteorol Soc 132(619):2009–2030
- Kosaka Y, Xie S-P, Lau N-C, Vecchi GA (2013) Origin of seasonal predictability for summer climate over the Northwestern Pacific. Proc Natl Acad Sci 110(19):7574–7579
- Lau KH, Lau N-C (1992) The energetics and propagation dynamics of tropical summertime synoptic-scale disturbances. Mon Weather Rev 120(11):2523–2539
- Lau N-C, Nath MJ (1996) The role of the "Atmospheric Bridge" in linking tropical Pacific ENSO events to extratropical SST anomalies. J Clim 9(9):2036–2057
- Lau N-C, Nath MJ (2009) A model investigation of the role of airsea interaction in the climatological evolution and ENSO-related variability of the summer monsoon over the South China Sea and Western North Pacific. J Clim 22(18):4771–4792
- Li SL, Lu J, Huang G, Hu KM (2008) Tropical Indian Ocean basin warming and East Asian summer monsoon: a multiple AGCM study. J Clim 21(22):6080–6088
- Matsuno T (1966) Quasi-geostrophic motions in the equatorial area. J Meteorol Soc Jpn 44(1):25–43
- North GR, Bell TL, Cahalan RF, Moeng FJ (1982) Sampling errors in the estimation of empirical orthogonal functions. Mon Weather Rev 110(7):699–706
- Rayner NA, Parker DE, Horton EB, Folland CK, Alexander LV, Rowell DP, Kent EC, Kaplan A (2003) Global analyses of sea surface temperature, sea ice, and night marine air temperature since the late nineteenth century. J Geophys Res 108(D14):4407. https://doi.org/10.1029/2002JD002670
- Rong X, Zhang R, Li T (2010) Impacts of Atlantic sea surface temperature anomalies on Indo-East Asian summer monsoon-ENSO relationship. Chin Sci Bull 55(22):2458–2468



- Simmons A, Wallace J, Branstator G (1983) Barotropic wave propagation and instability, and atmospheric teleconnection patterns. J Atmos Sci 40:1363–1392
- Srinivas G, Chowdary JS, Kosaka Y, Gnanaseelan C, Parekh A, Prasad KVSR (2018) Influence of the Pacific–Japan pattern on Indian summer monsoon rainfall. J Clim 31(10):3943–3958
- Stuecker MF, Timmermann A, Jin F, Mcgregor S, Ren H (2013) A combination mode of the annual cycle and the El Nino/Southern Oscillation. Nat Geosci 6(7):540
- Stuecker MF, Jin F-F, Timmermann A, McGregor S (2015) Combination mode dynamics of the anomalous Northwest Pacific anticyclone. J Clim 28(3):1093–1111
- Trenberth KE, Caron JM, Stepaniak DP, Worley S (2002) Evolution of El Niño-Southern Oscillation and global atmospheric surface temperatures. J Geophys Res Atmos 107(D8):AAC-5
- Wang B, Wu RG, Fu XH (2000) Pacific-East Asian teleconnection: how does ENSO affect East Asian climate? J Clim 13(9):1517–1536
- Wang B, Wu RG, Li T (2003) Atmosphere–warm ocean interaction and its impacts on Asian–Australian monsoon variation. J Clim 16(8):1195–1211
- Wang B, Yang J, Zhou TJ (2008) Interdecadal changes in the major modes of Asian–Australian monsoon variability: strengthening relationship with ENSO since the late 1970s. J Clim 21(8):1771–1789
- Watanabe M, Kimoto M (2000) Atmosphere-ocean thermal coupling in the North Atlantic: a positive feedback. Q J R Meteorol Soc 126:3343–3369
- Wu B, Li T, Zhou T (2010) Relative contributions of the Indian Ocean and local SST anomalies to the maintenance of the Western North Pacific anomalous anticyclone during the El Niño decaying summer. J Clim 23(11):2974–2986
- Xiang B, Wang B, Yu W, Xu S (2013) How can anomalous western North Pacific subtropical high intensify in late summer? Geophys Res Lett 40(10):2349–2354

- Xie S-P, Zhou Z-Q (2017) Seasonal modulations of El Niño-related atmospheric variability: Indo-Western Pacific Ocean feedback. J Clim 30(9):3461–3472
- Xie SP, Annamalai H, Schott FA, McCreary JP (2002) Structure and mechanisms of South Indian Ocean climate variability. J Clim 15(8):864–878
- Xie SP, Hu KM, Hafner J, Tokinaga H, Du Y, Huang G, Sampe T (2009) Indian Ocean capacitor effect on Indo-Western Pacific climate during the summer following El Nino. J Clim 22(3):730–747
- Xie SP, Du Y, Huang G, Zheng XT, Tokinaga H, Hu K, Liu Q (2010) Decadal shift in El Nino influences on Indo-Western Pacific and East Asian climate in the 1970s. J Clim 23:3352–3368
- Xie S, Kosaka Y, Du Y, Hu K, Chowdary JS, Huang G (2016) Indowestern Pacific ocean capacitor and coherent climate anomalies in post-ENSO summer: a review. Adv Atmos Sci 33(4):411–432
- Yang JL, Liu QY, Xie SP, Liu ZY, Wu LX (2007) Impact of the Indian Ocean SST basin mode on the Asian summer monsoon. Geophys Res Lett 34(2):L02708. https://doi.org/10.1029/2006GL028571
- Zhang R, Sumi A, Kimoto M (1996) Impact of El Niño on the East Asian monsoon: a diagnostic study of the '86/87 and '91/92 events. J Meteorol Soc Jpn 74(1):49–62
- Zhang W, Li H, Stuecker MF, Jin F, Turner AG (2016) A new understanding of El Niño's impact over East Asia: dominance of the ENSO combination mode. J Clim 29(12):4347–4359
- Zhou Z-Q, Xie S-P, Zhang GJ, Zhou W (2018) Evaluating AMIP skill in simulating interannual variability over the Indo-Western Pacific. J Clim 31(6):2253–2265

Publisher's Note Springer Nature remains neutral with regard to jurisdictional claims in published maps and institutional affiliations.

